



Experimental investigation of rotational vortex-induced vibrations of a circular cylinder attached to an elastic beam

Yaroslav Demchenko ^{a,b} *, Oleg Ivanov ^a , Vasily Vedenev ^{a,b} 

^a Institute of mechanics, Lomonosov Moscow State University, 1, Michurinskiy prospekt, Moscow, Russia

^b Faculty of Mechanics and Mathematics, Lomonosov Moscow State University, GSP-1, 1, Leninskie Gory, Moscow, Russia

ARTICLE INFO

Keywords:

Vortex-induced vibrations
Rotational oscillations
Translational oscillations
Circular cylinder
Vortex shedding

ABSTRACT

We study a rigid finite-span cylinder mounted on an elastic cantilever beam transversely to the direction of subsonic airflow in a wind tunnel. The purpose is to identify and analyze various types of vortex-induced resonant excitation for use in energy harvesters based on vortex-induced vibrations. The results of the experimental study show that in contrast to similar works with a similar model configuration that performs two-dimensional translational oscillations, we have discovered a previously unexplored three-dimensional type of VIV in which the cylinder rotates around the cantilever support. It has been experimentally proven that a lock-in regime exists for this type of oscillation, and the von Kármán vortex streets, generated by upper and lower parts of the cylinder, are shifted in phase by π . We conduct a detailed analysis of this new type of VIV.

1. Introduction

Vortex-induced vibrations (VIV) are a phenomenon of self-exciting oscillations of elastic or elastically mounted rigid bluff bodies exposed to a gas or fluid flow. They can be observed near chimneys, submarine pipelines and risers (Païdoussis et al., 2010). Body oscillations arise due to the lift force acting from the vortex structures formed downstream of the body, known as a von Kármán vortex street. For rigid cylinders with a wide range of Reynolds numbers $Re = U_\infty D_{ext}/\nu$, the vortex shedding frequency f_s satisfies the Strouhal–Reynolds number ($St - Re$) relationship with $St = f_s D_{ext}/U_\infty \approx const$. Here, U_∞ is the flow velocity, D_{ext} is the cylinder cross-section size, and ν is kinematic viscosity. In the case of circular cylinders, D_{ext} is the diameter, and the Strouhal number is close to 0.2 for the Reynolds number range from 300 to 2×10^5 , which is often called the subcritical range (Chen, 1987). However, for elastically mounted cylinders, when the vortex shedding frequency is close to the cylinder's natural frequency f_n , the phenomenon of synchronization or lock-in is observed (Griffin, 1985; Sarpkaya, 2004; Williamson and Govardhan, 2004). In this regime, vortex shedding frequency no longer satisfies $St \approx const$ and remains almost equal to the cylinder's natural frequency. Larger oscillation amplitudes are observed within the lock-in regime. In addition to the Strouhal number, the dimensionless reduced velocity is also used to characterize VIV, which is defined as $V_r = U_\infty/f_n D_{ext}$. Larger oscillation amplitudes result in wider lock-in ranges. The lock-in regime range of reduced velocities always includes a value corresponding to the inverse Strouhal number, near which the maximum amplitude is attained (Bearman, 1984). As the flow speed increases, the post-lock-in regime begins, which is characterized by the appearance of a jump in vortex shedding frequency, representing the end of the lock-in regime. In this regime, the vortex shedding frequency again satisfies $St \approx const$.

Bearman (1984), in his review of experimental studies related to vortex shedding, examined the mechanism of vortex shedding from the fixed bluff bodies. He stated that vortex shedding primarily occurs due to the interaction of two shear layers. Another

* Corresponding author at: Faculty of Mechanics and Mathematics, Lomonosov Moscow State University, GSP-1, 1, Leninskie Gory, Moscow, Russia.

E-mail address: demchenko@imec.msu.ru (Y. Demchenko).

<https://doi.org/10.1016/j.jfluidstructs.2025.104266>

Received 25 March 2024; Received in revised form 6 January 2025; Accepted 6 January 2025

0889-9746/© 2025 Elsevier Ltd. All rights are reserved, including those for text and data mining, AI training, and similar technologies.

important point discussed in his work is the absence of two-dimensionality in the vortices shed from a two-dimensional bluff body in uniform flow, i.e., the unsteady quantities related to vortex shedding are not constant along the body span. From Farivar (1981) work, it is also known that for a circular cylinder of finite span, the vortex shedding frequencies and the Strouhal number are lower in sections close to the end of the cylinder than for an infinitely long cylinder. In these sections, St is reduced to approximately 0.09–0.17. Thus, vortex shedding has a complex structure, even for fixed cylinders.

Vortex shedding from oscillating bodies is also a complex phenomenon. The vortex formed on the cylinder affects its motion, but at the same time, the movement of the cylinder changes the structure of the von Kármán vortex street. Williamson and Roshko (1988) found two regular vortex shedding modes and characterized each mode by the number of vortices: 2S, when two single vortices are shed from the cylinder per cycle of oscillations, and 2P, when two pairs of vortices are shed per cycle. Another mode of vortex shedding was discovered by Jauvtis and Williamson (2004) for the cylinder with two degrees of freedom, with shedding of two vortex triplets per cycle, named the 2T mode.

In a relatively recent work, Azadeh-Ranjbar et al. (2018) studied the VIV of finite-length circular cylinders with free ends and with different aspect-ratios AR, defined as the cylinder's length related to its diameter. They discovered that in the pre-lock-in and in post-lock-in regimes, the $St - Re$ relationship with $St \approx const$ remains but with a St smaller than 0.2, and the lower the AR, the lower the Strouhal number. The Strouhal number stays almost the same along the cylinder's span, but as it approaches the cylinder ends, it decreases. This effect occurs due to the presence of tip vortices because of the shear layer that separates from the cylinder ends (Zdravkovich et al., 1989). Azadeh-Ranjbar et al. (2018) also found that the reduced velocity value at peak amplitude increases approximately from 6.7 to 10.5 with a decrease in AR from 28.8 to 5.0. The response region of reduced velocities expands with decreasing AR.

The phase angle between lift force and cylinder deviation versus flow speed was plotted by Griffin et al. (1973). They showed that phase angle increases with increasing flow speed. Bearman and Currie (1979) subsequently confirmed this phase shift behavior. Sarpkaya (1978) studied time-dependent force acting on a rigid circular cylinder undergoing forced transverse oscillations in a uniform flow. He determined the in-phase and out-of-phase components of the force from experiments with Reynolds numbers in the range of $(5-25) \times 10^3$.

Over the past decades, the phenomenon of vortex-induced vibrations of circular cylinders has been actively used in the development of new types of wind generators (Bernitsas et al., 2008; Zhang and Wang, 2016; Adhikari et al., 2020; Wang et al., 2021; Zhang et al., 2021). Reviews on recent energy-harvesting models can be found in works of Abdelkefi (2016) and Wang et al. (2020). Depending on the oscillation amplitude, induction coils, magnets, and capacitive or piezoelectric transducers are used to convert mechanical energy into electrical energy (Li et al., 2016). Elahi et al. (2018) review the mechanisms of energy extraction and analyze existing piezoelectric electric power generators.

Since energy harvesting leads to effective additional damping in the oscillatory system, an important problem of finding ways to increase the intensity of oscillations arises. This can be ensured by an increase in their amplitude and frequency. To predict vortex-excited resonance characteristics, including oscillations amplitude, Griffin (1980) and Skop and Balasubramanian (1997) plotted the dimensionless transverse amplitude peak A_{max}/D_{ext} versus Skop–Griffin number $SG = 2\pi^3 m^* \zeta_s St^2$ (Griffin et al., 1975), known as a “Griffin plot”. Here, $\zeta_s = c/(2m_s(2\pi f_n))$ is the corresponding structural damping ratio, c is the structural damping, $m^* = m_s/m_a$ is the mass ratio, m_s is the structural mass, and m_a is the displaced fluid mass.

The following works observed regimes with increased amplitude. Khalak and Williamson (1996, 1999) showed that 2P vortex shedding mode for a low mass ratio corresponds to oscillation amplitudes of nearly one cylinder diameter D_{ext} . The corresponding branch of the amplitude response curve was called “upper branch”. Morse and Williamson (2009) showed that this mode related to upper branch was distinct from 2P mode corresponding to the lower branch. They suggested to call the vortex shedding mode related to the upper branch “2P₀ mode”. Moreover, Zhou et al. (1999) numerically showed that adding a streamwise degree of freedom to the cylinder increases the maximum amplitude compared to one-degree-of-freedom oscillations. Jauvtis and Williamson (2004) showed that in the 2T mode that exists for cylinder-mass ratios less than 6, the oscillation amplitude is nearly $1.5D_{ext}$; corresponding branch of the amplitude response curve was called “super-upper branch”. Azadeh-Ranjbar et al. (2018) for finite-length rigid circular cylinders obtained that with free ends, the lower the aspect-ratio AR in the response region, the higher the reduced velocity and the peak amplitude. Ivanov and Vedenev (2021) found that a 39% increase in oscillation amplitude was obtained for an elastic cylinder near a finite-length rigid plate compared to an isolated cylinder.

In the present work, the model of a circular cylinder attached to a flexible rectangular beam is studied. A similar configuration was considered by Dai et al. (2014), Azadeh-Ranjbar et al. (2018), Adhikari et al. (2020), and Zhang et al. (2021). In their experiments, no excitation of oscillations was observed out of the translational VIV mode's lock-in regime. However, in contrast to those works, we discovered a previously unexplored type of VIV in the post-lock-in regime region of translational oscillations. It is caused by resonance of the vortex street with rotational oscillations of the cylinder (Fig. 1), in which the beam performs torsional motion. For the experimental model under consideration in this regime, it turned out that the cylinder oscillates with a larger frequency and amplitude compared to the translational mode. If we proceed from the classical concept of vortex shedding, when the vortices along the cylinder span are shed approximately in phase, then rotational VIV cannot arise since the torque acting on the cylinder from the vortices is close to zero. Thus, it is suggested that during these three-dimensional rotational oscillations, the von Kármán vortex streets generated by the upper and lower parts of the cylinder are shifted in phase by π , and the transition from the upper to the lower cylinder segments occurs in the area of the attaching beam (acting as a splitter plate), which prevents vortex shedding at the cylinder center (Zhao, 2023). The main goal of the present paper is to analyze this new type of VIV.

The structure of the paper is as follows. In Section 2, we describe the problem statement. The derivation of the oscillation equations is given in Section 3. In Section 4, we describe the experimental setup and the model used in tests. In Section 5, we present the experimental results. Finally, Section 6 summarizes the results and concludes the paper.



Fig. 1. Two predominant types of oscillation: (a) translational and (b) rotational of a circular cylinder attached to a rectangular beam.

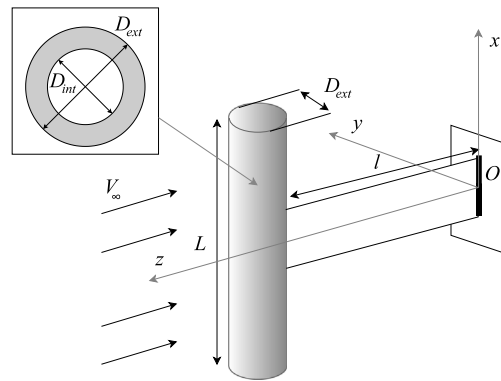


Fig. 2. Geometry of the experimental model.

2. Problem statement

Let us consider a rectangular elastic beam of length l , height a , and thickness b , which is rigidly embedded in a massive base, as shown in Fig. 2. The other end of the beam is rigidly embedded into a thin-walled rigid circular cylinder with length L , external diameter D_{ext} , and internal diameter D_{in} . Let us introduce a coordinate system, as shown in Fig. 2. The circular cylinder can perform plane-parallel translational motion in the Oyz plane, causing bending deformation of the beam. It can also rotate around the Oz axis, causing torsional deformation of the beam. Thus, there are two predominant types of motion: translational and rotational, as can be seen in Fig. 1. This system is excited by the uniform air flow moving opposite to the direction of the z -axis. As translational-type oscillations are a well-known phenomenon studied in detail by many authors, the main goal of the present study is the analysis of rotational oscillations, which are, to our knowledge, previously unexplored.

3. Equations of motion

3.1. Rotational oscillations

According to Timoshenko (1937), the equation of free torsional oscillations of the beam, under the assumptions of a small torsional rotation angle and the hypothesis of plane sections, is written in the form:

$$I_{m0} \frac{\partial^2 \theta}{\partial t^2} - \frac{\partial M_z}{\partial z} = 0, \quad M_z = GI \frac{\partial \theta}{\partial z} \tag{1}$$

where Oz is the elastic axis, z is the cross-section coordinate of the beam, t is time, G is the shear modulus, $\theta(z, t)$ is the torsional rotation angle (Fig. 3), I_{m0} is the cross-section mass polar moment of inertia about the elastic axis, M_z is the twisting moment, I is the torsion constant, and GI is the torsional stiffness.

In the case of a homogeneous beam with a constant rectangular cross-section, we have

$$I_{m0} \frac{\partial^2 \theta}{\partial t^2} - GI \frac{\partial^2 \theta}{\partial z^2} = 0, \tag{2}$$

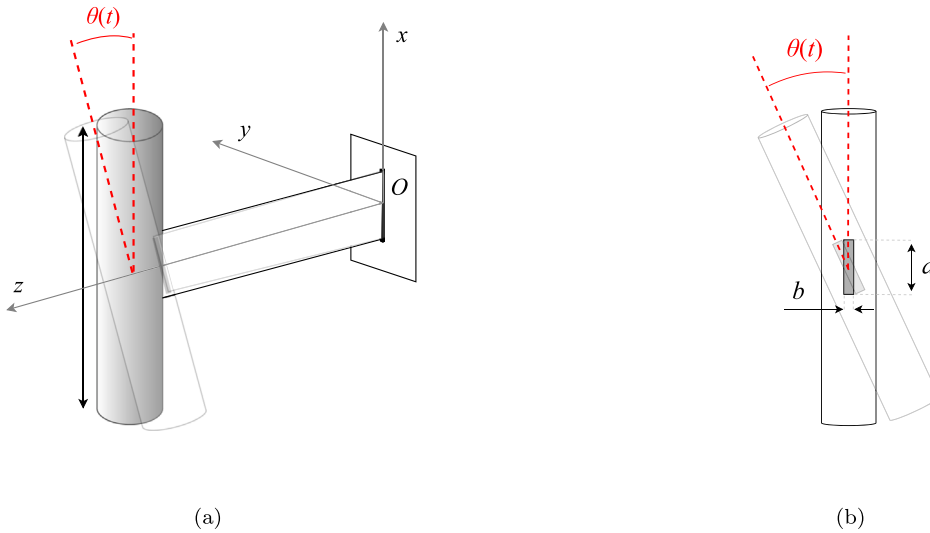


Fig. 3. Rotational oscillations of a circular cylinder attached to rectangular beam.

where $I = kab^3$ for $a \geq b$, $I_{m0} = \frac{1}{12} \rho ab (a^2 + b^2)$. Fig. 3 defines a and b , ρ is the beam material density. The value of the parameter k for a rectangular beam can be found in Ugural and Fenster (1975). Alternatively, the torsion constant I for $a \geq b$ can be calculated with an error of no more than 4% as follows (Young et al., 2012):

$$I \approx \frac{ab^3}{16} \left(\frac{16}{3} - 3.36 \frac{b}{a} \left(1 - \frac{b^4}{12a^4} \right) \right) \tag{3}$$

The equation of motion is supplemented with boundary conditions. The condition of a rigidly embedded end is equivalent to a rotation angle of zero at the attached point. The condition at the other end is described by the cylinder torque equation (Timoshenko, 1937). Thus, for a beam with one rigidly embedded end and a rigid body attached to the other end, we obtain:

$$\theta(0, t) = 0, \left[I_{cyl} \frac{\partial^2 \theta}{\partial t^2} + M_z \right] \Big|_{z=l} = 0. \tag{4}$$

Here, $I_{cyl} = m \cdot R_{ext}^2/2 + m \cdot L^2/12$ is the cylinder mass moment of inertia about the axis Oz , m is its mass, and $R_{ext} = D_{ext}/2$ and $R_{int} = D_{int}/2$ are the cylinder's external and internal radii, respectively.

3.2. Translational oscillations

We assume that all deviations from the equilibrium position are small. The position of the cylinder is determined by the angle $\alpha(t)$ of its deviation from the direction z and the coordinates $y_0(t)$, $z_0(t)$ of the instantaneous position of the beam's end. Therefore, we have

$$z_0(t) = l, y_0(t) = w(l, t), \tag{5}$$

where $w(z, t)$ is the neutral line of the beam's transverse deviation from the Oz axis (see Fig. 4). At point $z = l$, where the beam is rigidly embedded into the cylinder, the deflection angle $\alpha(t)$ must at any moment coincide with the beam's tangent at the point of their attachment, which is expressed by the relation

$$\frac{\partial w}{\partial z} \Big|_{z=l} = \alpha(t). \tag{6}$$

According to Timoshenko (1937), the equation for the beam's free-bending oscillations is written in the form

$$EJ \frac{\partial^4 w}{\partial z^4} + \rho S \frac{\partial^2 w}{\partial t^2} = 0, \tag{7}$$

where E is Young's modulus, J is the second moment of area of the beam's cross-section relative to the axis passing through the neutral line perpendicular to the Oyz plane, and $S = ab$ is the cross-sectional area of the beam.

The equation of motion is supplemented with boundary conditions. The condition of a rigidly embedded end is equivalent to the absence of deviation and deviation angle of zero at the attached point. The condition at the other end is formulated by the cylinder motion equation and torque equation. The Eq. (8) for the y -component of the velocity of the cylinder's center of mass v_{cyl} is obtained from Euler's formula

$$v_{cyl}(t) = \dot{w} \Big|_{z=l} + \dot{\alpha}(t) R_{ext}. \tag{8}$$

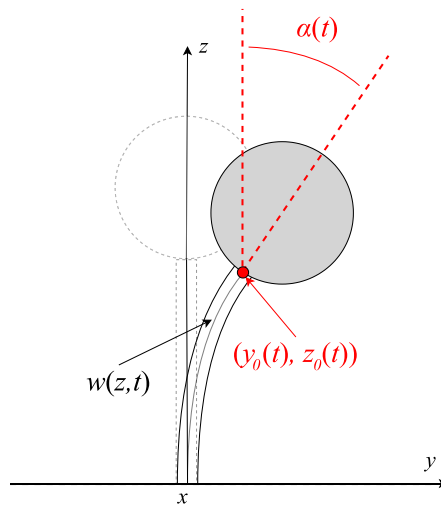


Fig. 4. Translational oscillations of a circular cylinder attached to a beam.

The bending moment M and shear force Q acting on the cylinder are determined as follows (Gere and Timoshenko, 1997):

$$M = EJ \frac{\partial^2 w}{\partial z^2}, Q = -EJ \frac{\partial^3 w}{\partial z^3}. \tag{9}$$

Thus, according to (8) and (9), we obtain the following boundary conditions:

$$\begin{aligned} z = 0 : w(0, t) = 0, \frac{\partial w}{\partial z} = 0, \\ z = l : m \dot{v}_{cyl} = -Q, J_0 \ddot{\alpha}(t) = -M - R_{ext} Q, \\ J_0 = \frac{m}{2} (R_{ext}^2 + R_{int}^2), J = \frac{ab^3}{12}, \end{aligned} \tag{10}$$

where J_0 is the circular cylinder moment of inertia about the cylinder axis.

3.3. Natural frequencies

Let us solve the homogeneous Eqs. (2) and (7) using the separation of variables method. We are looking for a solution in the form

$$\theta(z, t) = T_{rot}(t)Z_{rot}(z), w(z, t) = T_{tr}(t)Z_{tr}(z). \tag{11}$$

As a result, we have the following equations:

$$\begin{aligned} \ddot{T}_{rot}(t) + \omega_{rot}^2 T_{rot}(t) = 0, \ddot{T}_{tr}(t) + \omega_{tr}^2 T_{tr}(t) = 0, \\ Z''_{rot}(z) + n^2 Z_{rot}(z) = 0, Z_{tr}^{IV}(z) - k^4 Z_{tr}(z) = 0, \\ n = \omega_{rot} \sqrt{\frac{I_{m0}}{GI}}, k = \sqrt{\omega_{tr}^4 \frac{\rho S}{EJ}}. \end{aligned} \tag{12}$$

Solving the second equations, we get

$$\begin{aligned} Z_{rot}(z) = A \cos(nz) + B \sin(nz), \\ Z_{bend}(z) = C \operatorname{ch}(kz) + D \operatorname{sh}(kz) + E \cos(kz) + F \sin(kz). \end{aligned} \tag{13}$$

Substituting Eq. (13)'s first expression into the boundary conditions (4) leads to an eigenvalue problem for the unknown parameter n :

$$\cos(nl) - n \frac{I_{cyl}}{I_{m0}} \sin(nl) = 0, A = 0, B \neq 0. \tag{14}$$

The solution to this equation is a discrete set of eigenvalues:

$$n = n_1, n_2, n_3 \dots \tag{15}$$

Substituting Eq. (13)'s second expression into the boundary conditions (10) leads to a linear homogeneous system of equations for the coefficients $C, D, E,$ and F . For the system to have a nontrivial solution, its determinant must be equal to zero:

$$\begin{vmatrix} 1 & 0 & 1 & 0 \\ 0 & 1 & 0 & 1 \\ a_{31} & a_{32} & a_{33} & a_{34} \\ a_{41} & a_{42} & a_{43} & a_{44} \end{vmatrix} = 0. \quad (16)$$

Here, the matrix elements can be defined as:

$$\begin{aligned} a_{31} &= \text{ch}(kl) + \left[kR_{ext} + \frac{\rho S}{mk} \right] \text{sh}(kl), \\ a_{32} &= \text{sh}(kl) + \left[kR_{ext} + \frac{\rho S}{mk} \right] \text{ch}(kl), \\ a_{33} &= \cos(kl) - \left[kR_{ext} - \frac{\rho S}{mk} \right] \sin(kl), \\ a_{34} &= \sin(kl) + \left[kR_{ext} - \frac{\rho S}{mk} \right] \cos(kl), \\ a_{41} &= \text{ch}(kl) - \left[kR_{ext} + \frac{J_0}{\rho S} k^3 \right] \text{sh}(kl), \\ a_{42} &= \text{sh}(kl) - \left[kR_{ext} + \frac{J_0}{\rho S} k^3 \right] \text{ch}(kl), \\ a_{43} &= -\cos(kl) - \left[kR_{ext} - \frac{J_0}{\rho S} k^3 \right] \sin(kl), \\ a_{44} &= -\sin(kl) + \left[kR_{ext} + \frac{J_0}{\rho S} k^3 \right] \cos(kl). \end{aligned}$$

Thus, we obtain Eq. (16) for the unknown parameter k . The solution to this equation is a discrete set of eigenvalues:

$$k = k_1, k_2, k_3 \dots \quad (17)$$

The natural frequencies of the system are determined using (12)'s last expressions. For the first translational and rotational circular ω and physical σ natural frequencies, which are our interest, we obtain:

$$\begin{aligned} \omega_{tr} &= k_1^2 \sqrt{\frac{EJ}{\rho S}}, \sigma_{tr} = \frac{k_1^2}{2\pi} \sqrt{\frac{EJ}{\rho S}} \\ \omega_{rot} &= n_1 \sqrt{\frac{GI}{I_{m0}}}, \sigma_{rot} = \frac{n_1}{2\pi} \sqrt{\frac{GI}{I_{m0}}} \end{aligned} \quad (18)$$

4. Experimental setup

Experiments were conducted in the Institute of Mechanics of Lomonosov Moscow State University in wind tunnel A-10 with an Eiffel chamber and an open test section. The test section of the octagonal cross-section (Fig. 5) was 800 mm in height and 1360 mm in length. A beam with a 3×33 mm cross-section was made of steel with density $\rho = 7850$ kg/m³, Young's modulus $E = 224 \times 10^9$ Pa, and shear modulus $G = 82 \times 10^9$ Pa. Two beams of lengths $l = 325$ mm and $l = 375$ mm were tested. The cylinder was made of duralumin with mass $m_s = 0.116$ kg (the corresponding mass ratio $m^* \approx 386$), length $L = 500$ mm, external diameter $D_{ext} = 25$ mm, and internal diameter $D_{int} = 23$ mm. The operating Reynolds numbers range was $(1 - 9.3) \times 10^3$.

A Riftek RF-603 triangulation laser sensor was used to measure the deviations of the cylinder's top end 5 mm from the tip (Fig. 5(b) and 6(a)). The sensor was fixed in space, and its measurements were recorded at a sampling rate of 8 kHz. Note that in rotational VIV mode, the tip of the cylinder moves along an arc, so the measurement point changed slightly during the period of rotational oscillations. However, due to the small rotation angle values, the error in amplitude measurements was less than 1%. A Smart Sensor AR866 hot-film anemometer was installed in the undisturbed flow to measure the flow speed. The measurement error for both sensors was less than 1%. A mirror was installed on the elastic beam to identify the oscillation type based on the reflection of a trace caused by a laser pointer (Fig. 6(a)): horizontal and vertical traces are caused by bending and torsional beam deformations, respectively. The flow velocity fluctuations behind the cylinder were measured by a DISA 55DO5 constant temperature anemometer (CTA) with a hot-wire probe 55P81 (Fig. 6(b)) at a sampling rate of 8 kHz and a recording duration of 20 sec. The probe was located at a distance of two diameters in the streamwise direction and one diameter in the transverse direction from the cylinder axis (Fig. 6(a)). We measured the flow velocity fluctuations by using one probe sequentially in different cross-sections at distances of $\pm 25, \pm 50, \pm 100,$ and ± 150 mm from the Oz axis. The natural frequencies and damping ratios of both types of oscillations were measured by free oscillation tests in still air. The translational and rotational natural frequencies f_{tr} and f_{rot} measured were 12.67 Hz and 27.62 Hz for a beam of length 325 mm, and 10.10 Hz and 25.60 Hz for a beam of length 375 mm, respectively. Damping ratios ζ_{tr} and ζ_{rot} , corresponding to translational and rotational oscillations, were also measured for both beam lengths. The theoretical natural frequencies were calculated using Eqs. (18). The values of these quantities are given in Table 1. It is seen that the theoretical frequencies are in reasonable agreement with the measured values.

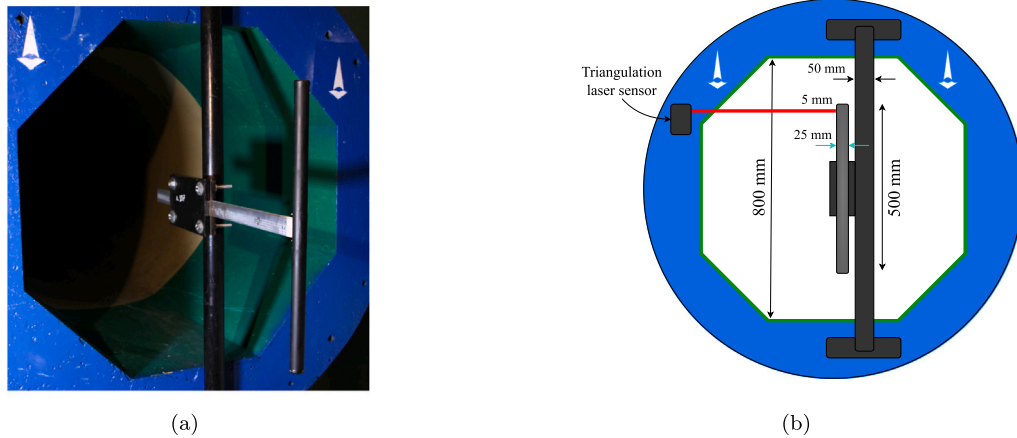


Fig. 5. Experimental equipment. (a) The circular cylinder on the transverse rectangular beam in the wind tunnel, (b) the geometric properties of the experimental facility.

Table 1
Natural oscillations parameters.

l , mm	f_{tr} , Hz	σ_{tr} , Hz	ζ_{tr}	f_{rot} , Hz	σ_{rot} , Hz	ζ_{rot}
325	12.67	14.46	0.011	27.62	27.93	0.012
375	10.10	11.37	0.011	25.60	25.99	0.011

5. Results

5.1. Vortex shedding analysis for a fixed cylinder

In the first series of experiments, the vortex shedding frequency f_s was measured for a fixed cylinder with a beam length l of 325 mm sequentially at heights of ± 25 , ± 50 , ± 100 , and ± 150 mm from the Oz axis. As can be seen from Fig. 7, the vortex shedding frequency nearly satisfies $St \approx 0.16$, which correlates well with the experimental results of Azadeh-Ranjbar et al. (2018). The decrease in the Strouhal number compared to infinite-span cylinders is associated with the presence of tip vortices because of the shear layer that separates from the cylinder ends (Zdravkovich et al., 1989).

5.2. Amplitude response for both oscillation types

The cylinder was unfixed in subsequent experiments. As a result of the second series of experiments, the oscillation amplitudes A versus the flow speed U_∞ and the dimensionless amplitude A/D_{ext} versus reduced velocity V_r were plotted for the two beam lengths. Initially, with an increase in flow speed, the excitation of translational oscillations occurred; with a subsequent increase in speed, the oscillations became rotational (Fig. 8(a)). The shift in the amplitude response towards higher flow speeds is explained by the difference in natural frequencies. But in terms of dimensionless parameters, the amplitude peaks correspond to close reduced velocities. Note that since there are two different types of oscillations, we have calculated the reduced velocity using two different natural frequencies f_{tr} , and f_{rot} , corresponding to translational and rotational VIV (Table 1). The amplitude response shows maximum oscillation amplitude for both oscillation types in a reduced velocity range of 6.1–7.2 (Fig. 8(b)), which corresponds to a Strouhal number of 0.164–0.139. These values correlate well with Azadeh-Ranjbar et al. (2018) results for translational VIV using a similar model. It can be seen that the amplitude of rotational VIV turned out to be more than twice as large as translational VIV. The peak amplitudes of classical quasi-two-dimensional translational oscillations versus SG are plotted in Fig. 8(c); they correlate quite well with the Griffin plot (Griffin, 1980; Skop and Balasubramanian, 1997). It should be noted that the amplitude of rotational VIV is a function of the cylinder cross-section coordinate x . To avoid x -dependence, the deviation angle of the cylinder θ can be taken as a characteristic of the amplitude of rotational VIV. The maximum amplitude of rotational VIV corresponds to an angle of 0.029 rad for a beam length of 325 mm, and 0.034 rad for a beam length of 375 mm. This parameter, however, was not used in Figs. 8 and 9, because it does not make sense for translational VIV.

5.3. Lock-in regime

The third set of experiments aimed to analyze the flow downstream of the cylinder for both types of VIV using the synchronous recordings of the triangulation laser sensor and constant temperature anemometer. The beam length l was 325 mm, and the probe was located sequentially at heights of ± 25 , ± 50 , ± 100 , and ± 150 mm from the Oz axis. This experiment demonstrates the existence

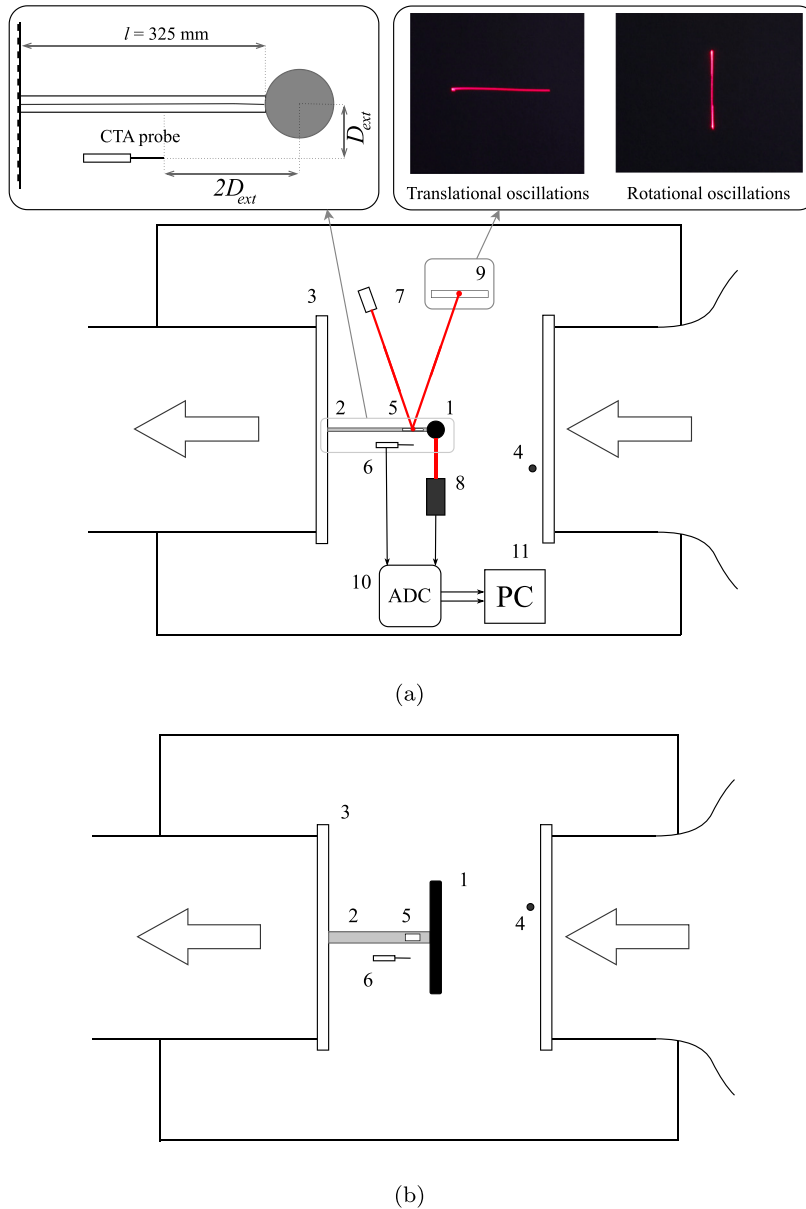


Fig. 6. Experimental scheme: (a) top view, (b) side view. (1) Circular cylinder, (2) rigidly embedded beam, (3) rigid massive base, (4) hot-film anemometer, (5) mirror, (6) CTA probe, (7) laser pointer, (8) triangulation laser sensor, (9) screen, (10) analog-to-digital converter (ADC), (11) PC. A laser pointer trace reflected in a mirror determines the oscillation type.

of 5 regimes (Fig. 9(c)). Pre- and post-lock-in regimes correspond to modes for which the vortex shedding frequency nearly satisfies $St \approx 0.16$. The translational lock-in regime corresponds to classical VIV observed by Azadeh-Ranjbar et al. (2018). As can be seen from Figs. 9(c) and 9(d), there is also a lock-in regime for rotational VIV, which we call “rotational lock-in”. In this regime, the oscillation amplitude of the cylinder tips is greater than translational lock-in. The existence of two VIV modes can be useful in the design of VIV-based energy harvesters. Finally, the transition regime corresponds to the mode between translational and rotational lock-in regimes, where vortex shedding frequency satisfies $St \approx const$. In terms of dimensionless parameters, the data from lock-in regions (Fig. 9(c)) can be represented as follows: the ratio f_s/f_{tr} versus reduced velocity V_r as shown in Fig. 9(d), where V_r was calculated differently for translational and rotational VIV with corresponding structural frequencies taken as a frequency scale. It can be seen that the vortex shedding frequency for rotational lock-in is more than twice as large as for translational lock-in, whereas lock-in V_r ranges are close. Spectral analysis of the CTA signal showed that in the lock-in regions the predominant frequency practically coincided with the natural frequency and there is no double frequency. Thus, the vortex shedding corresponded to the 2S mode.

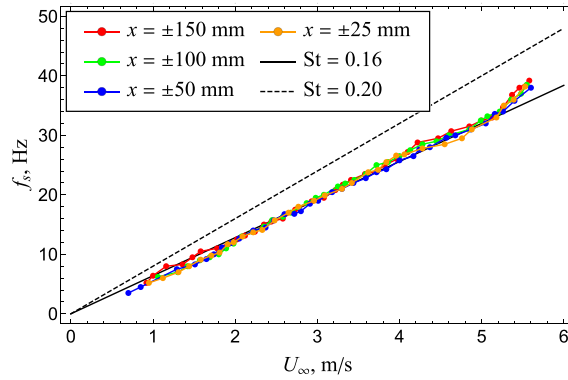


Fig. 7. Vortex shedding frequency f_s (Hz) for the fixed cylinder versus flow speed U_∞ (m/s) for a beam length of 325 mm and anemometer height locations of ± 25 , ± 50 , ± 100 , and ± 150 mm from the axis of rotation.

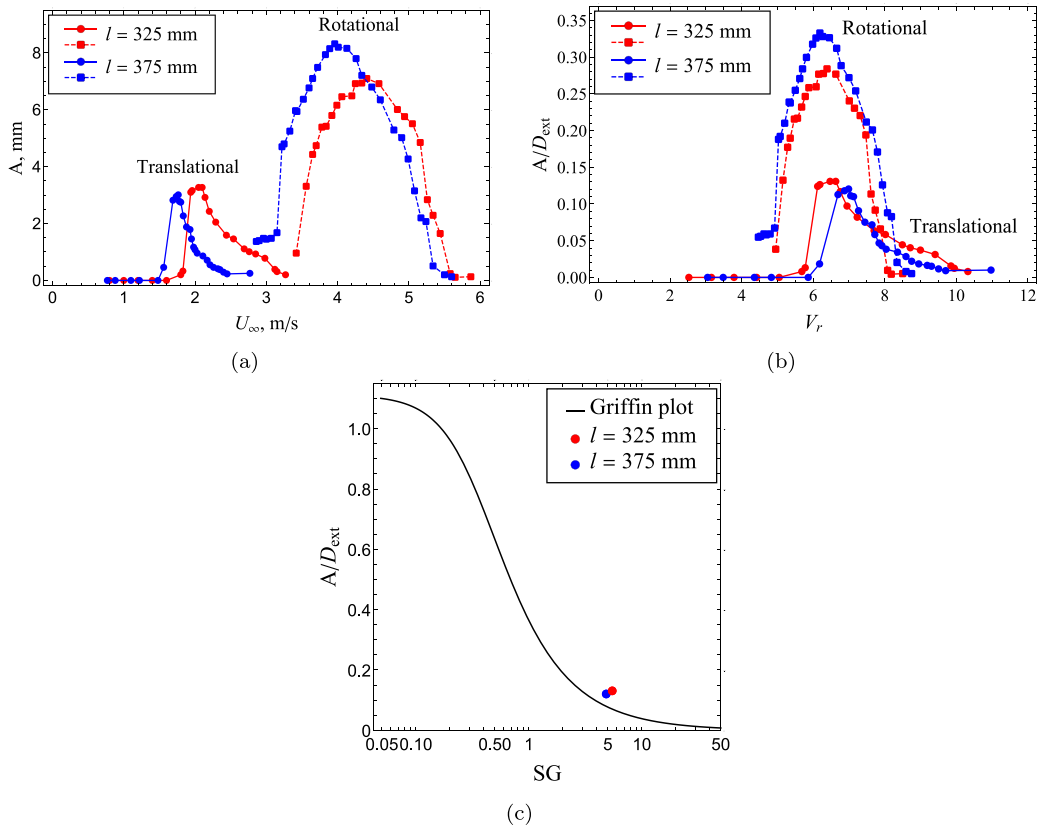


Fig. 8. (a) Oscillation amplitude A (mm) versus flow speed U_∞ (m/s) for two beam lengths, (b) dimensionless amplitude A/D_{ext} versus reduced velocity V_r ; (c) Griffin plot with points corresponding to peak amplitudes of translational oscillations. Circular and square markers correspond to translational and rotational oscillations, respectively.

5.4. Phase shift analysis

The third series of experiments was also devoted to analyzing the phase shift between the cylinder position and the vortex shed. The anemometer signal was bandpass-filtered in a range of $f_{ir} \pm 0.1$ Hz and $f_{rot} \pm 0.1$ Hz, where f_{ir} and f_{rot} are natural frequencies taken from Table 1. To calculate the phase shift φ between the flow velocity fluctuations and deviation of the cylinder, the correlation between these signals was used, which is defined by Eq. (19):

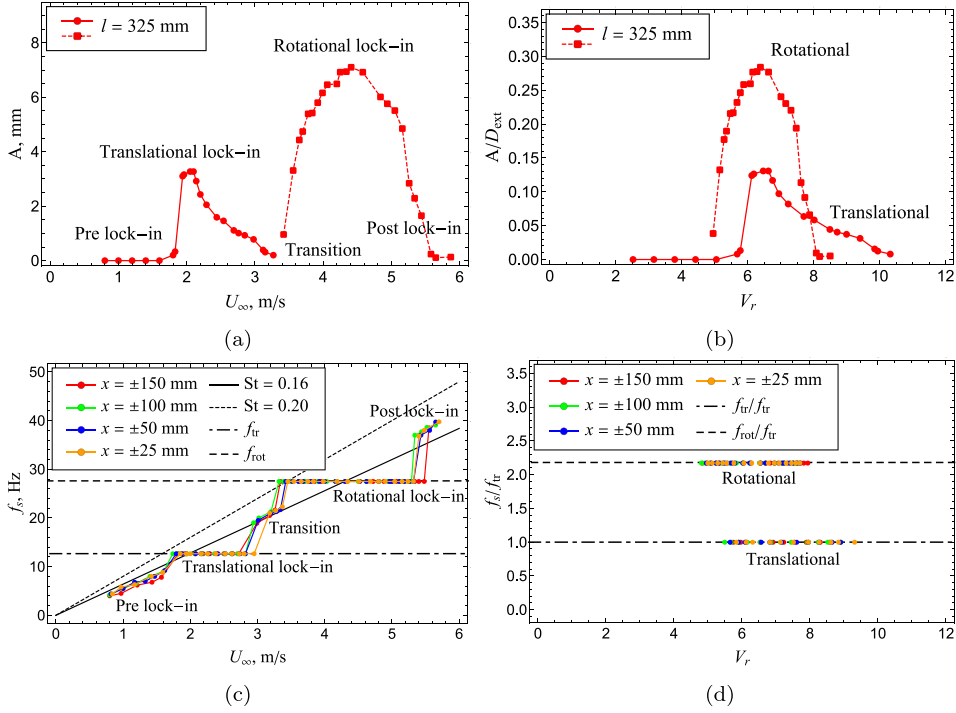


Fig. 9. Amplitude response and vortex shedding frequency evolution for a beam length of 325 mm. (a) Oscillation amplitude A (mm) and (c) vortex shedding frequency f_s (Hz) versus flow speed U_∞ (m/s), (b) dimensionless amplitude A/D_{ext} and (d) f_s/f_{tr} ratio versus reduced velocity V_r in lock-in regions. The markers for the amplitude response graphs are similar to Fig. 8.

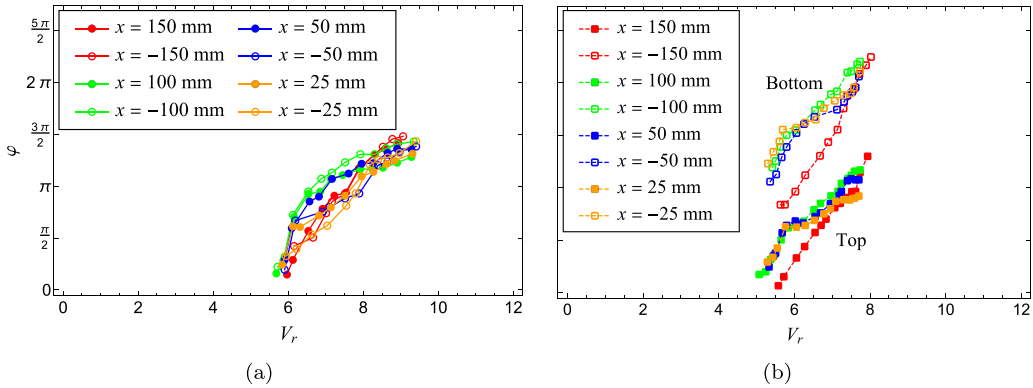


Fig. 10. Phase shift φ between the signals of anemometer and triangulation laser sensor versus reduced velocity V_r for a beam length of 325 mm and anemometer height locations of ± 25 , ± 50 , ± 100 , and ± 150 mm from axis of rotation. (a) Translational lock-in, (b) rotational lock-in. Circular and square markers correspond to translational and rotational oscillations, respectively; filled markers and empty markers correspond to top and bottom cross-sections, respectively.

$$\text{corr} = \frac{\sum_{i=1}^N w_i s_i}{\sqrt{\sum_{i=1}^N w_i^2 \sum_{i=1}^N s_i^2}}, \quad (19)$$

where w_i is a time series of the cylinder deviations from the equilibrium position, s_i is a filtered time series of the flow velocity fluctuations, and N is the number of measurements. For two periodic functions $q(t) = q_0 \cos(\omega t)$, $u(t) = u_0 \cos(\omega t + \varphi)$, the continuous representation of correlation function is

$$\text{corr} = \frac{\int_0^T q u dt}{\sqrt{\int_0^T q^2 dt \int_0^T u^2 dt}} \rightarrow \cos \varphi, \text{ as } T \rightarrow \infty, \quad (20)$$

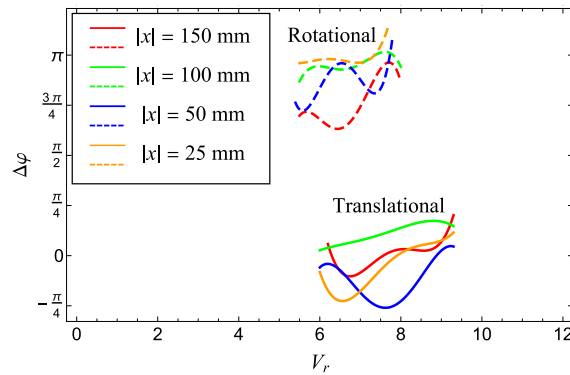


Fig. 11. Phase shift differences $\Delta\varphi = \varphi_{\text{bottom}} - \varphi_{\text{top}}$ for the opposite sections located at the same distance from the rotation axis versus reduced velocity V_r .

where ω is a circular frequency and T is the averaging time. The arccos function is used to calculate the phase shift φ between two functions. Since the sign of φ is not recovered by this method, we assume that $w_i = w_i^0 \cos(\omega t)$, $s_i = s_i^0 \cos(\omega t + \varphi)$, and the sign was determined by direct comparison of these two signals. The resulting phase shift is shown in Fig. 10. These data sets were then fitted with a fourth-degree polynomial using the least squares method. Finally, phase shift differences $\Delta\varphi = \varphi_{\text{bottom}} - \varphi_{\text{top}}$ between the von Kármán vortex streets in cross-sections located symmetrically relative to the Oz axis were calculated (Fig. 11).

As can be seen in Fig. 10, the phase shift increases along with reduced velocity for both types of oscillations. The phase shifts are almost the same for symmetrical cross-sections across the response region for translational VIV, i.e., the von Kármán vortex street is close to two-dimensional (Figs. 10 and 11). However, for rotational VIV, the phase at the top and bottom parts of the cylinder differ by approximately π , i.e., they are opposite to each other. Moreover, the phase abruptly changes when passing through cross-sections of the beam (which acts like a splitter plate). Thus, the beam prevents the vortex shedding and splits the flow into two “subflows”, in which the vortex shedding occurs in the antiphase.

6. Discussion and conclusions

We have studied the dynamics of a rigid, thin-walled, finite-span cylinder mounted on an elastic cantilever beam in a wind tunnel. Two modes of VIV were observed: classical quasi-two-dimensional VIV and a previously unknown rotational type. In the first mode, the beam experiences bending oscillations, and the cylinder performs two-dimensional translational motion. The second mode is caused by the resonance of the vortex street with the rotational oscillations of the cylinder, in which the beam performs torsional motion. To our knowledge, rotational VIV in such an experimental scheme has not been observed in the literature before, so this discovery is this study’s primary finding. During these three-dimensional VIV, a lock-in regime exists and the von Kármán vortex streets generated by the upper and lower parts of the cylinder, are shifted in phase by approximately π . The phase change occurs abruptly near the beam, which acts as a splitter plate and prevents vortex shedding from the central sections.

The maximum amplitude of rotational VIV at the cylinder ends $A/D_{\text{ext}} = 0.34$ was obtained in the present experiments. In this regime, the characteristic reduced velocity range is 6–7.2, which corresponds to a Strouhal number of 0.166–0.139. These values are smaller than $St \approx 0.2$ for two-dimensional vortex shedding, which is explained by the finite span of the cylinder in the present experiments. The amplitude of rotational VIV turned out to be more than twice as large as that of classical quasi-two-dimensional translational VIV, which suggests more effective energy harvesting from the rotational oscillations.

The excitation of the rotational mode clearly yields the variable oscillation amplitude along the cylinder span. It is somewhat similar to the oscillations of tapered cylinders studied by Techet et al. (1998) and Hover et al. (1998). In both cases, the non-dimensional oscillation amplitude A/D varies over the span. In Techet et al. (1998) study, this yields the existence of a “hybrid” vortex shedding mode, 2S, over one part of the cylinder and 2P over the other part. In the present study, such a hybrid mode was not observed, and the mode was always 2S. However, a sort of hybrid vortex shedding mode might exist for longer cylinder lengths with a larger range of non-dimensional amplitudes, which could be a matter for future study.

The non-symmetric tapering of the cylinder in our configuration could also facilitate the excitation of the rotational mode. When the translational oscillation mode is excited, the vortex shedding occurs in a quasi-two-dimensional form, which does not generate torque on the cylinder. It is thus necessary to reconfigure the vortex street to be in anti-phase at two sides of the cylinder to support rotational oscillations. Non-symmetric tapering of the cylinder would additionally provoke the rotational mode and reconfiguration of the vortex street since the torque would be non-zero even in a pure translational mode.

In future studies of rotational VIV, it would be interesting to analyze whether they occur without a splitter plate, which seems to be a crucial point for the abrupt change of the vortex shedding phase, which, in turn, supports excitation of the rotational mode. Also, it may seem that increase in the length of the beam, which decreases the pivotal stiffness, would lead to an increase in the amplitude of the cylinder tip. However, the work done by fluid force over the oscillation cycle at the end sections will be negative if the amplitude is too large (Morse and Williamson, 2009). This will lead to a decrease in the amplitude of oscillations in terms of

rotation angle, if the pivotal stiffness is sufficiently small. Hence, there should exist a limit in the amplitude growth as the pivotal stiffness decreases. Optimal pivotal stiffness can be a matter of a future study. Another problem worth of study is the influence of the cylinder's length on the tip amplitudes and the angle of cylinder rotation, with the goal of maximizing the amplitudes by selecting the appropriate length.

CRedit authorship contribution statement

Yaroslav Demchenko: Writing – original draft, Investigation. **Oleg Ivanov:** Writing – review & editing, Methodology, Investigation. **Vasily Vedeneev:** Writing – review & editing, Supervision, Methodology, Conceptualization.

Declaration of competing interest

The authors declare that they have no known competing financial interests or personal relationships that could have appeared to influence the work reported in this paper.

Acknowledgments

This paper is dedicated to the memory of Sergey V. Guvernuyuk, the initiator of this study. Our numerous scientific discussions and his support of this and other works will always stay in our memory. The authors are grateful to Alexander F. Zubkov for his help with the initial stage of this research. The work is supported by the Ministry of Science and Higher Education of the Russian Federation within the Program of Center “Supersonic” (agreement 075-15-2022-331, April 26, 2022).

Data availability

Data will be made available on request.

References

- Abdelkefi, A., 2016. Aeroelastic energy harvesting: A review. *Internat. J. Engrg. Sci.* 100, 112–135. <http://dx.doi.org/10.1016/J.IJENGSCI.2015.10.006>.
- Adhikari, S., Rastogi, A., Bhattacharya, B., 2020. Piezoelectric vortex induced vibration energy harvesting in a random flow field. *Smart Mater. Struct.* 29 (3), <http://dx.doi.org/10.1088/1361-665X/ab519f>.
- Azadeh-Ranjbar, V., Elvin, N., Andreopoulos, Y., 2018. Vortex-induced vibration of finite-length circular cylinders with spanwise free-ends: Broadening the lock-in envelope. *Phys. Fluids* 30 (10), 105104. <http://dx.doi.org/10.1063/1.5042774/990150>.
- Bearman, P., 1984. Vortex shedding from oscillating bluff bodies. *Annu. Rev. Fluid Mech.* 16 (1), 195–222. <http://dx.doi.org/10.1146/annurev.fl.16.010184.001211>.
- Bearman, P., Currie, I., 1979. Pressure-fluctuation measurements on an oscillating circular cylinder. *J. Fluid Mech.* 91 (4), 661–677. <http://dx.doi.org/10.1017/S0022112079000392>.
- Bernitsas, M., Raghavan, K., Ben-Simon, Y., Garcia, E., 2008. VIVACE (Vortex Induced Vibration Aquatic Clean Energy): A new concept in generation of clean and renewable energy from fluid flow. *J. Offshore Mech. Arct. Eng.* 130 (4), <http://dx.doi.org/10.1115/1.2957913>.
- Chen, S.-S., 1987. *Flow Induced Vibration of Circular Cylindrical Structures*. Hemisphere Publishing Corporation, New York, <https://archive.org/details/flowinducedvibra0000chen>.
- Dai, H., Abdelkefi, A., Wang, L., 2014. Piezoelectric energy harvesting from concurrent vortex-induced vibrations and base excitations. *Nonlinear Dynam.* 77 (3), 967–981. <http://dx.doi.org/10.1007/s11071-014-1355-8>.
- Elahi, H., Eugeni, M., Gaudenzi, P., 2018. A review on mechanisms for piezoelectric-based energy harvesters. *Energies* 11 (7), 1850. <http://dx.doi.org/10.3390/EN11071850>.
- Farivar, D., 1981. Turbulent uniform flow around cylinders of finite length. *AIAA J.* 19, 275281, <https://arc.aiaa.org/doi/10.2514/3.7771>.
- Gere, J., Timoshenko, S., 1997. *Mechanics of Materials*. PWS Pub Company, Boston, pp. 599–680, <https://archive.org/details/mechanicsofmater00gere>.
- Griffin, O., 1980. Vortex-excited cross-flow vibrations of a single cylindrical tube. *J. Press. Vessel. Technol.* 102 (2), 158–166. <http://dx.doi.org/10.1115/1.3263315>.
- Griffin, O., 1985. Vortex shedding from bluff bodies in a shear flow: A review. *J. Fluids Eng.* 107 (3), 298–306. <http://dx.doi.org/10.1115/1.3242481>.
- Griffin, O., Skop, R., Koopmann, G., 1973. Measurements of the response of bluff cylinders to flow-induced vortex shedding. In: *Proceedings of the Annual Offshore Technology Conference, 1973-April*. pp. 1767–1778. <http://dx.doi.org/10.4043/1814-MS>.
- Griffin, O., Skop, R., Ramberg, S., 1975. The resonant, vortex-excited vibrations of structures and cable systems. In: *Proceedings of the Annual Offshore Technology Conference, 1975-May*. pp. 731–736. <http://dx.doi.org/10.4043/2319-MS>.
- Hover, F., Techet, A., Triantafyllou, M., 1998. Forces on oscillating uniform and tapered cylinders in cross flow. *J. Fluid Mech.* 363, 97–114, <https://www.cambridge.org/core/journals/journal-of-fluid-mechanics/article/forces-on-oscillating-uniform-and-tapered-cylinders-in-cross-flow/71AEAB01790BFCC19F6DF29E81911AC3>.
- Ivanov, O., Vedeneev, V., 2021. Vortex-induced vibrations of an elastic cylinder near a finite-length plate. *J. Fluids Struct.* 107, <http://dx.doi.org/10.1016/j.jfluidstruct.2021.103393>.
- Jauvtis, N., Williamson, C., 2004. The effect of two degrees of freedom on vortex-induced vibration at low mass and damping. *J. Fluid Mech.* 509, 23–62. <http://dx.doi.org/10.1017/S0022112004008778>.
- Khalak, A., Williamson, C., 1996. Dynamics of a hydroelastic cylinder with very low mass and damping. *J. Fluids Struct.* 10 (5), 455–472. <http://dx.doi.org/10.1006/jfls.1996.0031>.
- Khalak, A., Williamson, C., 1999. Motions, forces and mode transitions in vortex-induced vibrations at low mass-damping. *J. Fluids Struct.* 13 (7–8), 813–852. <http://dx.doi.org/10.1006/jfls.1999.0236>.
- Li, D., Wu, Y., da Ronch, A., Xiang, J., 2016. Energy harvesting by means of flow-induced vibrations on aerospace vehicles. *Prog. Aerosp. Sci.* 86, 28–62. <http://dx.doi.org/10.1016/J.PAEROSCI.2016.08.001>.

- Morse, T., Williamson, C., 2009. Prediction of vortex-induced vibration response by employing controlled motion. *J. Fluid Mech.* 634, 5–39. <http://dx.doi.org/10.1017/S0022112009990516>.
- Paidoussis, M., Price, S., De Langre, E., 2010. *Fluid–Structure Interactions: Cross-Flow-Induced Instabilities*. Cambridge University Press.
- Sarpkaya, T., 1978. Fluid forces on oscillating cylinders. *J. Waterw., Port Coast. Ocean. Div.* 104 (3), 275–290. <http://dx.doi.org/10.1061/JWPCDX.0000101>.
- Sarpkaya, T., 2004. A critical review of the intrinsic nature of vortex-induced vibrations. *J. Fluids Struct.* 19 (4), 389–447. <http://dx.doi.org/10.1016/J.JFLUIDSTRUCTS.2004.02.005>.
- Skop, R., Balasubramanian, S., 1997. A new twist on an old model for vortex-excited vibrations. *J. Fluids Struct.* 11 (4), 395–412. <http://dx.doi.org/10.1006/JFLS.1997.0085>.
- Techet, A., Hover, F., Triantafyllou, M., 1998. Vortical patterns behind a tapered cylinder oscillating transversely to a uniform flow. *J. Fluid Mech.* 363, 79–96. <https://www.cambridge.org/core/journals/journal-of-fluid-mechanics/article/vortical-patterns-behind-a-tapered-cylinder-oscillating-transversely-to-a-uniform-flow/2B1A30D5F86E5FAF9F086834D1DC05F5>.
- Timoshenko, S., 1937. *Vibration Problem in Engineering*. D. Van Nostrang Company, INC., New York, pp. 325–333. <https://archive.org/details/in.ernet.dli.2015.78232>.
- Ugural, A., Fenster, S., 1975. *Advanced Strength and Applied Elasticity*. American Elsevier Pub. Co., New York. https://archive.org/details/advancedstrength00ugur_0.
- Wang, J., Geng, L., Ding, L., Zhu, H., Yurchenko, D., 2020. The state-of-the-art review on energy harvesting from flow-induced vibrations. *Appl. Energy* 267, 114902. <http://dx.doi.org/10.1016/J.APENERGY.2020.114902>.
- Wang, J., Gu, S., Abdelkefi, A., Bose, C., 2021. Enhancing piezoelectric energy harvesting from the flow-induced vibration of a circular cylinder using dual splitters. *Smart Mater. Struct.* 30 (5), <http://dx.doi.org/10.1088/1361-665X/abefb5>.
- Williamson, C., Govardhan, R., 2004. Vortex-induced vibrations. *Annu. Rev. Fluid Mech.* 36, 413–455. <http://dx.doi.org/10.1146/annurev.fluid.36.050802.122128>.
- Williamson, C., Roshko, A., 1988. Vortex formation in the wake of an oscillating cylinder. *J. Fluids Struct.* 2 (4), 355–381. [http://dx.doi.org/10.1016/S0889-9746\(88\)90058-8](http://dx.doi.org/10.1016/S0889-9746(88)90058-8).
- Young, W., Budynas, R., Sadegh, A., 2012. *Roark's Formulas for Stress and Strain*, eighth ed. McGraw Hill, New York.
- Zdravkovich, M., Brand, V., Weston, A., Mathew, G., 1989. Flow past short circular cylinders with two free ends. *J. Fluid Mech.* 203 (557), 557–575. <http://dx.doi.org/10.1017/S002211208900159X>.
- Zhang, M., Wang, J., 2016. Experimental study on piezoelectric energy harvesting from vortex-induced vibrations and wake-induced vibrations. *J. Sens.* 2016, <http://dx.doi.org/10.1155/2016/2673292>.
- Zhang, M., Zhang, C., Abdelkefi, A., Yu, H., Gaidai, O., Qin, X., Zhu, H., Wang, J., 2021. Piezoelectric energy harvesting from vortex-induced vibration of a circular cylinder: Effect of Reynolds number. *Ocean Eng.* 235, 109378. <http://dx.doi.org/10.1016/J.OCEANENG.2021.109378>.
- Zhao, M., 2023. A review of recent studies on the control of vortex-induced vibration of circular cylinders. *Ocean Eng.* 285, 115389. <http://dx.doi.org/10.1016/J.OCEANENG.2023.115389>.
- Zhou, C., So, R., Lam, K., 1999. Vortex-induced vibrations of an elastic circular cylinder. *J. Fluids Struct.* 13 (2), 165–189. <http://dx.doi.org/10.1006/JFLS.1998.0195>.